Atmos. Meas. Tech., 3, 733–749, 2010
www.atmos-meas-tech.net/3/733/2010/
doi:10.5194/amt-3-733-2010

Atmospheric Measurement Techniques

Theoretical description of functionality, applications, and limitations of SO_2 cameras for the remote sensing of volcanic plumes

C. Kern, F. Kick, P. Lübcke, L. Vogel, M. Wöhrbach, and U. Platt

Institute for Environmental Physics, University of Heidelberg, Im Neuenheimer Feld 229, 69120 Heidelberg, Germany

Received: 22 January 2010 – Published in Atmos. Meas. Tech. Discuss.: 12 February 2010
Revised: 25 May 2010 – Accepted: 2 June 2010 – Published: 29 June 2010

Abstract. The SO_2 camera is a novel device for the remote sensing of volcanic emissions using solar radiation scattered in the atmosphere as a light source for the measurements. The method is based on measuring the ultra-violet absorption of SO_2 in a narrow wavelength window around 310 nm by employing a band-pass interference filter and a 2 dimensional UV-sensitive CCD detector. The effect of aerosol scattering can in part be compensated by additionally measuring the incident radiation around 325 nm, where the absorption of SO_2 is about 30 times weaker, thus rendering the method applicable to optically thin plumes. For plumes with high aerosol optical densities, collocation of an additional moderate resolution spectrometer is desirable to enable a correction of radiative transfer effects. The ability to deliver spatially resolved images of volcanic SO_2 distributions at a frame rate on the order of 1 Hz makes the SO_2 camera a very promising technique for volcanic monitoring and for studying the dynamics of volcanic plumes in the atmosphere.

This study gives a theoretical basis for the pertinent aspects of working with SO_2 camera systems, including the measurement principle, instrument design, data evaluation and technical applicability. Several issues are identified that influence camera calibration and performance. For one, changes in the solar zenith angle lead to a variable light path length in the stratospheric ozone layer and therefore change the spectral distribution of scattered solar radiation incident at the Earth's surface. The varying spectral illumination causes a shift in the calibration of the SO_2 camera's results. Secondly, the lack of spectral resolution inherent in the measurement technique leads to a non-linear relationship between measured weighted average optical density and the SO_2 column density. Thirdly, as is the case with all remote sensing techniques that use scattered solar radiation as a light source, the radiative transfer between the sun and the instrument is variable, with both "radiative dilution" as well as multiple scattering occurring. These effects can lead to both, over or underestimation of the SO_2 column density by more than an order of magnitude. As the accurate assessment of volcanic emissions depends on our ability to correct for these issues, recommendations for correcting the individual effects during data analysis are given.

Aside from the above mentioned intrinsic effects, the particular technical design of the SO_2 camera can also greatly influence its performance, depending on the setup chosen. A general description of an instrument setup is given, and the advantages and disadvantages of certain specific instrument designs are discussed. Finally, several measurement examples are shown and possibilities to combine SO_2 camera measurements with other remote sensing techniques are explored.

Correspondence to: C. Kern
(ckern@iup.uni-heidelberg.de)

1 Introduction

SO_2 is widely monitored at actively degassing volcanoes, since its emission flux can be used as a proxy for the degassing magma volume, and its long atmospheric lifetime (of the order of days) makes it an ideal benchmark for studying other, less stable species (Oppenheimer et al., 1998b, Bobrowski et al., 2003; McGonigle et al., 2004; Rodríguez et al., 2008). A number of measurement techniques exist, but ever since the first application of the correlation spectrometer (COSPEC) to volcanic emissions measurements (Moffat

Published by Copernicus Publications on behalf of the European Geosciences Union.

and Millán, 1971; Stoiber et al., 1983), remote sensing techniques have become more and more established. More recently, the introduction of miniature ultra-violet spectrometers to the field (Galle et al., 2002; Edmonds et al., 2003) has reduced both the cost and complexity of such measurements, and applying the well-established retrieval techniques of differential optical absorption spectroscopy (DOAS) is now standard practice (Platt and Stutz, 2008). Aside from the obvious advantage of being able to measure volcanic emissions from a safe distance, it is also possible to implement measurement geometries that allow the retrieval of the total volcanic emission flux of a species, assuming lossless transport to the point of measurement (e.g. Galle et al., 2002, 2009; McGonigle et al., 2005).

The relatively high spectral resolution (typically below 1 nm) of the DOAS instruments allows the simultaneous retrieval of different trace gas species. Aside from SO_2, both BrO and NO_2 have been detected in volcanic plumes in the past using scattered light DOAS observations (e.g. Bobrowski et al., 2003; Oppenheimer et al., 2005). Fourier transform infrared spectroscopy (FTIR) and active long-path DOAS can measure even more species in the IR and deep UV spectral ranges (Oppenheimer et al., 1998a; Burton et al., 2007; Kern et al., 2009), but they require more complex measurement geometries, as radiation at these wavelength ranges is not readily available in scattered sunlight.

The COSPEC and DOAS measurements allow determination of the trace gas column density in a single direction only, or rather in a typically small (of the order of 10^{-4} steradian) element of solid angle, although at typically high sensitivity and (in the case of DOAS) high specificity. Obviously one- or two-dimensional (2-D) "images" of the plume are highly desirable for a variety of reasons (see below and Mori and Burton, 2006 and Bluth et al., 2007). First attempts to obtain 2-D trace gas images (of NO_2, SO_2 and BrO) in the UV used the Imaging-DOAS (I-DOAS) approach (Lohberger et al., 2004; Bobrowski et al., 2006; Louban et al., 2009), where a column of image pixels is simultaneously recorded by an imaging spectrometer. A 2-D image is then constructed by scanning the viewing direction perpendicular to this column. While the I-DOAS technique appears to combine the advantages of DOAS with imaging capabilities, the price to be paid is a relatively long acquisition time (of the order of 15 min for a single image) and relatively complex setup of the instrument. As the dynamic process governing the propagation and dispersal of volcanic plumes in the atmosphere occur on significantly shorter time scales (order of seconds), a simpler and faster means of recording 2-D images of volcanic gases is desirable.

The large amounts of SO_2 present in volcanic plumes and the fact that SO_2 is by far the most dominant absorber around 300 nm, however, make high spectral resolution measurements unnecessary for the quantification of SO_2 alone. Mori and Burton, 2006 and Bluth et al., 2007 have demonstrated the ability to measure 2-D SO_2 distributions in volcanic plumes using a simple UV-sensitive camera and band-pass filters only transmitting radiation at wavelengths significantly influenced by SO_2 absorption. Here, this concept is first dealt with in a theoretical approach. Certain problems are identified, and methods for improving both the accuracy and technical implementation of the technique are described. Finally, some examples of the discussed methods and applications are shown.

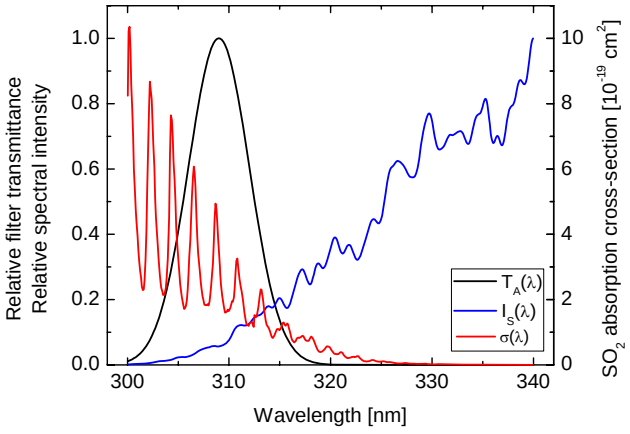

Fig. 1. Example of the spectral transmittance $T(\lambda)$ of a band-pass filter which could be used in a SO_2 camera setup. In this case, the maximum transmittance is centered at 309 nm, a region in which the SO_2 absorption-cross-section $\sigma(\lambda)$ is prominent (Bogumil et al., 2003). Also shown in blue is an example spectrum of incident scattered solar radiation $I_S(\lambda)$, in this case measured with an Ocean Optics© USB2000 spectrometer at 0.7 nm resolution.

2 Measurement principle

In its simplest form, an SO_2 camera is solely composed of a UV sensitive camera and a single spectral band-pass filter (referred to as filter A in the following) allowing only radiation in a narrow wavelength interval encompassing significant SO_2 absorption structures to enter the camera optics. Figure 1 shows an example of the transmittance curve $T_A(\lambda)$ of such a band-pass filter along with the absorption cross-section $\sigma(\lambda)$ of SO_2. For each pixel, the intensity signal collected through this filter is compared to a background intensity, either measured in a region in which no plume is present or interpolated from values acquired on either side of the plume.

In the absence of SO_2, the wavelength-dependent light intensity $I_{0,A}(\lambda)$ arriving at each pixel of the 2-D camera CCD is given by the intensity of scattered solar radiation $I_S(\lambda)$ arriving at the instrument (see Fig. 1), the filter transmittance $T_A(\lambda)$, and the quantum efficiency $Q(\lambda)$ of the detector.

$$I_{0,A}(\lambda) = I_S(\lambda) \cdot T_A(\lambda) \cdot Q(\lambda) \quad (1)$$

If SO_2 is present in the optical path of the incident radiation, the spectral intensity is attenuated according to the Beer-Lambert-Bouguer law.

$$I_A(\lambda) = I_{0,A}(\lambda) \cdot \exp(-\sigma(\lambda) \cdot S(\lambda)) \quad (2)$$

Here, $\sigma(\lambda)$ is the absorption cross-section of SO_2 and $S(\lambda)$ is its column density, or the integral of the SO_2 concentration along the effective light path L (ideally the line of sight through the plume).

$$S(\lambda) = \int_L c(x)\, dx \quad (3)$$

Unfortunately, the effective light path L can deviate substantially from the line of sight through the plume. Especially in cases where volcanic plumes contain large amounts of SO_2 or scattering aerosols or are viewed from a large distance, the effective light path may be significantly shorter or longer than a straight line through the area of interest. Radiation entering the field of view between the plume and the instrument ("radiative dilution") shortens the effective light path, while multiple scattering inside the plume elongates it. In fact, the absorption of radiation by SO_2 in volcanic plumes is oftentimes sufficiently strong in itself to influence the effective light path. Therefore, the column density S is typically a function of the wavelength λ. All of these effects were recently described and quantified by Kern et al. (2010), along with a suggested method for their correction using moderate resolution spectral data obtained from a DOAS instrument.

The negative logarithm of $I(\lambda)/I_0(\lambda)$ gives the optical density $\tau(\lambda)$, which is directly proportional to the SO_2 column density $S(\lambda)$ if SO_2 absorption is the only cause of light attenuation at the wavelength λ along the effective optical path.

$$\tau(\lambda) = -\ln\left(\frac{I_A(\lambda)}{I_{0,A}(\lambda)}\right) = \sigma(\lambda) \cdot S(\lambda) \quad (4)$$

A spectroscopic instrument with sufficient resolution would measure the optical density $\tau(\lambda)$ to retrieve the column density S, but the SO_2 camera instead measures the integral $I_{M,A}$ of the incident intensity $I_A(\lambda)$ over the transmission range of the filter (the subscript A denotes intensities after having passed filter A as stated above).

$$I_{M,A} = \int_\lambda I_A(\lambda)\, d\lambda \quad (5)$$

The respective relation is valid for the background measurement $I_{N,A}$, although measuring this parameter can be difficult (see Sect. 2.2).

$$I_{N,A} = \int_\lambda I_{0,A}(\lambda)\, d\lambda \quad (6)$$

From these measured quantities, the weighted average optical density $\hat{\tau}_A$ is retrieved.

$$\hat{\tau}_A = -\ln\left(\frac{I_{M,A}}{I_{N,A}}\right) = \ln\left(I_{N,A}\right) - \ln\left(\int_\lambda I_{0,A}(\lambda) \cdot \exp(-\sigma(\lambda) \cdot S) \cdot d\lambda\right) \quad (7)$$

Using the notation defined in Eq. (1) and (2), the weighted average optical density $\hat{\tau}_A$ is given by

$$\hat{\tau}_A = -\ln\left(\frac{\int_\lambda I_S(\lambda) \cdot T_A(\lambda) \cdot Q(\lambda) \cdot \exp(-\sigma(\lambda) \cdot S(\lambda)) \cdot d\lambda}{\int_\lambda I_S(\lambda) \cdot T_A(\lambda) \cdot Q(\lambda) \cdot d\lambda}\right) \quad (8)$$

While the weighted average optical density $\hat{\tau}_A$ is obviously a function of the SO_2 column density S, it is important to note that the dependency of $\hat{\tau}_A$ on S is generally non-linear (i.e. $\hat{\tau}_A(S_2) < (S_2/S_1) \cdot \hat{\tau}_A(S_1)$ if $S_1 < S_2$). Only if the filter wavelength transmittance range is sufficiently narrow that the SO_2 cross-section σ and the column density S can be regarded as independent of the wavelength λ in the measurement window can the integrated optical density be written as

$$\hat{\tau}_A = -\ln\left(\frac{I_{N,A} \cdot \exp(-\sigma \cdot S)}{I_{N,A}}\right) = \sigma \cdot S = \tau \quad (9)$$

In this exceptional case, the weighted average optical density $\hat{\tau}_A$ would be equal to the optical density τ of SO_2 at the measurement wavelength and is therefore proportional to the column density S. Then the instrument is in principle calibration free, as the relationship between the measured value $\hat{\tau}_A$ and the column density S is defined by Eq. (9) (where $\sigma(\lambda)$ is known from laboratory measurements).

In all other cases, Eq. (8) cannot easily be solved for the column density S because the incident scattered solar radiation spectrum $I_S(\lambda)$, the filter spectral transmittance $T_A(\lambda)$ and the quantum yield of the detector $Q(\lambda)$ are not well known. They must either be accurately measured (which is especially difficult for $I_S(\lambda)$, as it is constantly changing and needs to be measured behind the plume) or an empirical instrument calibration must be conducted to determine the relationship between the weighted average optical density $\hat{\tau}_A$ and the SO_2 column density S. This has been done with mixed success in the past (see Mori and Burton, 2006; Bluth et al., 2007, Kick, 2008; Wöhrbach, 2008). The theoretical description given above now allows analysis of where problems with calibration lie and how these can be solved (see Sect. 2.3). First, however, the concept of normalized optical density is discussed.

2.1 Normalized optical density/apparent absorbance

In general, the relationship between the measured weighted average optical density $\hat{\tau}_A$ and the column density S of SO_2 is complex (see Eq. 8), but an empirical calibration can greatly simplify the data evaluation process. However, one condition that must be fulfilled for the measurement principle described in Sect. 2 to remain valid is that the SO_2 absorption is the only parameter influencing light attenuation in the transmitting wavelength window of the applied filter A. While this condition may approximately be fulfilled in the case of cloudless skies and translucent, aerosol-free (non-condensing) volcanic plumes (see Bluth et al., 2007; Mori and Burton, 2009), it will not generally be valid. In the presence of aerosols (water droplets or ash) in the volcanic plume, radiation entering the plume from behind will in part be scattered out of the instrument's field of view, thus causing a decrease in intensity. On the other hand, light entering the plume from other angles will in part be scattered towards the instrument, thereby causing an increase in intensity. Depending on the single scattering albedo of the plume aerosols, radiation will also be absorbed to some degree by the particles. Finally, a species other than SO_2 could be present in the plume and also absorb light in the measurement wavelength window. All of these processes compete with one another and can lead to attenuation or enhancement of radiation intensity being emitted from the plume towards the instrument when compared to the background sky intensity. If the measurement principle described in Sect. 2 is simply applied, each of these influences will distort the retrieved weighted average optical density $\hat{\tau}_A$ and therefore the SO_2 column density S.

Fortunately, in contrast to the SO_2 absorption, which is by far the strongest in the UV-wavelengths between about 250 and 320 nm (see Fig. 1 and Bogumil et al., 2003), aerosol scattering and absorption processes are of a broad-band nature, i.e. they are only weakly dependent on wavelength. Therefore, a second band-pass filter with a transmittance window above 320 nm, in the following referred to as filter B, can be used to quantify the amount of light attenuation (or enhancement) not originating from SO_2 absorption. Mori and Burton, 2006 successfully applied this technique at Sakurakima volcano in 2005. In this approach, band-pass filter A on the SO_2 camera is at times replaced by filter B. Both background ($I_{N,B}$) and plume images ($I_{M,B}$) are recorded through filter B. Before the weighted average optical density $\hat{\tau}_A$ is calculated, the ratio of pixel intensities measured through filter A ($I_{M,A}/I_{N,A}$) is normalized by the ratio of pixel intensities measured through filter B ($I_{M,B}/I_{N,B}$). Likewise, the weighted average optical density $\hat{\tau}_B$ can be calculated and subtracted from the optical density $\hat{\tau}_A$. The thus retrieved value is the normalized optical density $\hat{\tau}$, sometimes also referred to as the apparent absorbance AA.

$$\hat{\tau} = AA = -\ln\left(\frac{I_{M,A}/I_{N,A}}{I_{M,B}/I_{N,B}}\right) = \ln\left(\frac{I_{M,A}/I_{M,B}}{I_{N,A}/I_{N,B}}\right) \quad (10)$$
$$= \hat{\tau}_A + \ln\left(I_{M,B}/I_{N,B}\right) = \hat{\tau}_A - \hat{\tau}_B$$

Because of its greatly improved robustness in regard to the influence of scattering and broadband absorption effects, normalizing the optical density is necessary whenever a significant aerosol load is present or water condensation occurs in a volcanic plume.

Obviously, this approach assumes that the influence of aerosol scattering on the measured intensities is equal in both observed wavelength ranges. As typical Ångstrom exponents of volcanic aerosols lie between 0 and approximately 2 (e.g. Spinetti and Buongiornio, 2007), depending on their size distributions, the maximum error associated with this assumption is about 10%, and typical errors are around 5%. However, the radiative transfer between the sun and the instrument can be dramatically changed by aerosols in the volcanic plume, thus possibly changing the effective light path by 70% or more (Kern et al., 2010). This needs to be taken into account when calculating concentrations or fluxes from the measured optical densities. The condition that SO_2 must be the dominant narrow-band absorber in the filter A wavelength window remains a prerequisite for an accurate retrieval of the SO_2 column density S.

2.2 Obtaining the background intensity

The measurement principle of the SO_2 camera is based on the ability to calculate the SO_2 column density S from the optical density τ (see Eq. 4). Due to the finite bandwidth of the applied interference filters, only a weighted average optical density $\hat{\tau}_A$ can be determined (Eq. 7). However, the background intensity I_N at each pixel of the image is a also needed for the retrieval. Obtaining this background image is often difficult, as an image of exactly the observed scene in absence of the volcanic plume is in principle required, as shown in Fig. 2.

Since this is usually impossible to obtain, one approach is to approximate the background intensity I_N by recording an image next to the volcanic plume. This approach works well for low solar zenith angles and if the background is homogeneous i.e. in the absence of clouds. However, as both the Rayleigh and Mie scattering phase functions are not spherically symmetric, recording of a background image in a different viewing direction than the one in which the plume measurement is performed at will inevitably yield a different intensity distribution, especially for high solar zenith angles. In particular when the sun is close to the horizon, the radiation intensity recorded in a specific azimuthal direction relative to north can differ by a factor of up to 2 from the intensity

recorded at 90° azimuth relative to this direction, simply because of the non-isotropic Rayleigh phase function.

A second approach to obtaining an appropriate background image is to interpolate intensity values obtained on either side of the plume during the plume measurement. This method has the advantage that it is not necessary to pan the camera's viewing direction. Considering the fact that a frequent recording of the background image is favorable because it is influenced by solar zenith angle and aerosol/cloud conditions, this method is clearly advantageous. However, the technique also has a drawback: when using the first approach, a sophisticated flat-field correction is not necessary, as differences in radiation sensitivity across the detector (e.g. caused by optical vignetting, pixel quantum efficiency, and varying filter illumination angle, see Sect. 2.3) cancel out when calculating the normalized optical density according to Eq. 10. Only the detector offset and dark current, which can both easily be measured by taking dark images, need to be corrected. In this second approach, however, an accurate flat-field correction must be applied to any images before the background intensity can be interpolated from the pixels on either side of the plume. Therefore, it is necessary to carefully characterize the relative sensitivity of each pixel on the detector. This can e.g. be achieved in the laboratory by measuring a homogeneously illuminated surface but is difficult to perform in the field.

2.3 Calibration issues

While the normalization of the integrated optical density is an important concept for the correction of broad-band light attenuation, the issue of how to derive the SO_2 column density S from the observed optical density $\hat{\tau}$ remains. Although it is in principle possible to construct a version of the SO_2 camera with inherent calibration by using very narrow band-pass filters (or possibly an interferometer), the transmittance window width would need to be on the order of 0.1 nm to ensure that the SO_2 absorption cross-section can be assumed to be constant in the transmittance window (see Eq. 8). However, such a design greatly reduces the instrument light throughput and therefore the measurement signal-to-noise ratio. For an optimal SO_2 sensitivity, the ideal band-pass filter transmittance $T(\lambda)$ is considerably wider, as is shown in Sect. 3.2. In the past, calibration of the SO_2 camera has typically been conducted prior to or after measurements were made by inserting various SO_2 calibration cells with known SO_2 column densities S into the instrument's field of view and determining an empirical relationship between the normalized optical density $\hat{\tau}$ (or apparent absorbance AA) and the SO_2 column density S (see e.g. Dalton et al., 2009; Mori and Burton, 2009). Because the normalized optical density $\hat{\tau}$ depends on the incident scattered solar radiation spectrum $I_S(\lambda)$, the spectral transmittance of the band-pass filters $T(\lambda)$, and the quantum efficiency of the detector $Q(\lambda)$ (see Eq. 8), this simple approach will only function properly if all three parameters are constant in time. Unfortunately, this is usually not the case. While the quantum efficiency $Q(\lambda)$ can be assumed more or less constant in time and independent of wavelength in the region of interest, the other two parameters can vary depending on the measurement conditions and chosen optical setup.

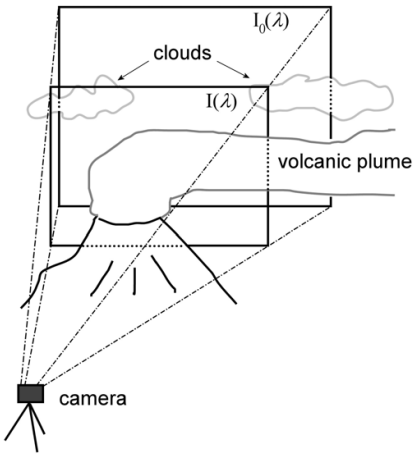

Fig. 2. Schematic of the SO_2 camera measurement geometry. The intensity of incident radiation $I(\lambda)$ is measured in and around the volcanic plume. In order to calculate the SO_2 optical density $\tau(\lambda)$ from which the SO_2 column density is derived, however, information about the background intensity $I_0(\lambda)$ is needed (see Eq. 4). This information can be difficult to obtain, especially if the illumination conditions behind the plume are inhomogeneous e.g. due to the presence of clouds.

In the following, a model was applied to study the sensitivity of the SO_2 camera to variations in the spectral distribution of the incident scattered solar radiation $I_S(\lambda)$ and filter transmittance $T(\lambda)$. The transmittance of the band-pass filter A was simulated using a Gaussian transmittance distribution centered at λ_C = 309 nm and with a standard deviation of 3 nm (or FWHM of approximately 8 nm, shown in Fig. 1). This curve closely resembles the transmittance curve of the filter later chosen for the construction of the SO_2 camera prototype (compare Fig. 9). For each wavelength between 300 and 340 nm, the measured incident scattered solar radiation spectrum $I_S(\lambda)$ was multiplied by the filter transmittance $T_A(\lambda)$. The quantum efficiency $Q(\lambda)$ was not taken into account further, as the quantum efficiency of the spectrometer's detector is intrinsically included in the measured solar spectrum $I_S(\lambda)$ and is thought to closely resemble that of a typical SO_2 camera. In this manner, the spectral intensity $I_{0,A}(\lambda)$ was calculated according to Eq. (1). The calculation was then repeated, this time including SO_2 absorption by multiplying with the exponential function given in Eq. (2), assuming an SO_2 column density of 1×10^{18} molec/cm^2 or 400 ppmm. This is a typical value for volcanic gas emissions measurements.

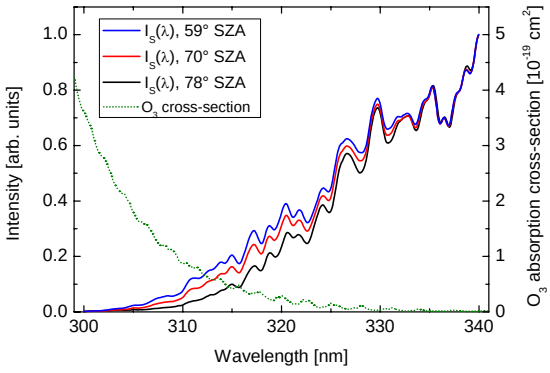

Fig. 3. Measured spectra of scattered solar radiation $I_S(\lambda)$ for three different solar zenith angles (SZA). While an absolute calibration was not achieved (the quantum yield $Q(\lambda)$ of the spectrometer is unknown), the intensity between 300 and 340 nm obviously increases relative to the intensity at 340 nm with decreasing solar zenith angle. This is caused by a decrease in optical path length of the detected radiation in the ozone layer. The ozone absorption cross-section (shown as dotted line) increases sharply towards lower wavelengths (Voigt et al., 2001, 223 K).

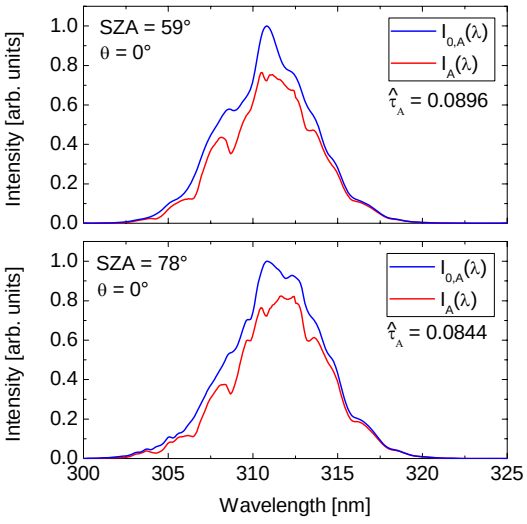

Fig. 4. Modeled light intensity I_A passing filter A of the UV-camera as a function of wavelength λ for two different solar zenith angles (SZA). The blue curve ($I_{0,A}$) assumes no SO_2 in the optical path (background spectrum), while the red curve (I_A) represents an SO_2 column density S of 400 ppmm. In both cases, light passes the filter in a perpendicular direction ($\theta = 0$). The ratio of integrated intensity under the background spectrum and under the measurement spectrum yields the indicated integrated optical density $\hat{\tau}_A$ according to Eq. (7). The two weighted average optical densities $\hat{\tau}_A$ differ by 6%, even though the assumed SO_2 column density S was the same in both cases.

2.3.1 Effect of the incident spectral intensity distribution

The spectrum of scattered radiation arriving at the earth's surface depends on the solar zenith angle (SZA), especially in the UV wavelength region. For high solar zenith angles, the average optical path length through the stratospheric ozone layer is considerably longer than for lower SZAs.[1] As the ozone absorption cross-section increases dramatically towards deep UV wavelengths (see Fig. 3), the lower end of the scattered light spectrum is particularly influenced by these variations in optical path length.

In Figure 3, measurements of the incident scattered radiation spectrum $I_S(\lambda)$ made in Heidelberg, Germany on a cloudless day are shown. Three spectra were recorded at 59, 70, and 78° SZA, respectively. Each spectrum was normalized to its intensity at 340 nm. While all spectra fall off to null at approximately 300 nm, their relative intensities vary across the wavelength range from 300 to 340 nm, a result of variations in ozone optical density.

Using these measured spectra and the model described above, the effect of such variations on the weighted average SO_2 optical density $\hat{\tau}$ measured with an SO_2 camera can be discussed. In this first study, the spectral intensities $I_{0,A}(\lambda)$ and $I_A(\lambda)$ were calculated using the incident spectral intensities measured at the solar zenith angles 59° and 78°. The four curves calculated in this manner are shown in Fig. 4. The presence of Fraunhofer absorption lines and, in the case of $I_A(\lambda)$, superimposed SO_2 absorption lines makes for a highly variable spectral distribution which peaks around 311 nm even though the maximum filter transmission is located at 309 nm.

The SO_2 camera, however, does not measure the spectral intensities $I(\lambda)$, but only the integrated intensities $I_{M,A}$ and $I_{N,A}$ defined in Eq. (5 and 6). These can be calculated from the distributions shown in Fig. 4 by integrating the spectral intensities $I(\lambda)$ over the transmittance range of the filter. Then, the weighted average optical density $\hat{\tau}_A$ can be calculated according to Eq. (7). The obtained values for the integrated optical density $\hat{\tau}_A$ are given below the legends in Fig. 4. For the assumed measurement conditions, the two values differ by 6%. At higher solar zenith angles, the error will become even larger. This example therefore illustrates the fact that a correct calibration of the measured weighted average optical density $\hat{\tau}_A$ will depend on the solar zenith angle at the time of the measurement. In fact, a variation in the total stratospheric ozone column will have the same effect, as the total O_3 column density along the optical path determines the spectrum $I_S(\lambda)$. The use of a correction factor for this effect is non-trivial, however, as the magnitude of the correction will depend on other factors as well, including the SO_2 column density S itself.

[1] There is one exception to this rule. For SZAs approaching 90° the average optical path through the ozone layer decreases. This so-called Umkehr-Effect (Götz, 1931; Götz et al., 1934) is caused by an increase in the contribution of radiation scattered above the ozone layer to the total incident scattered light.

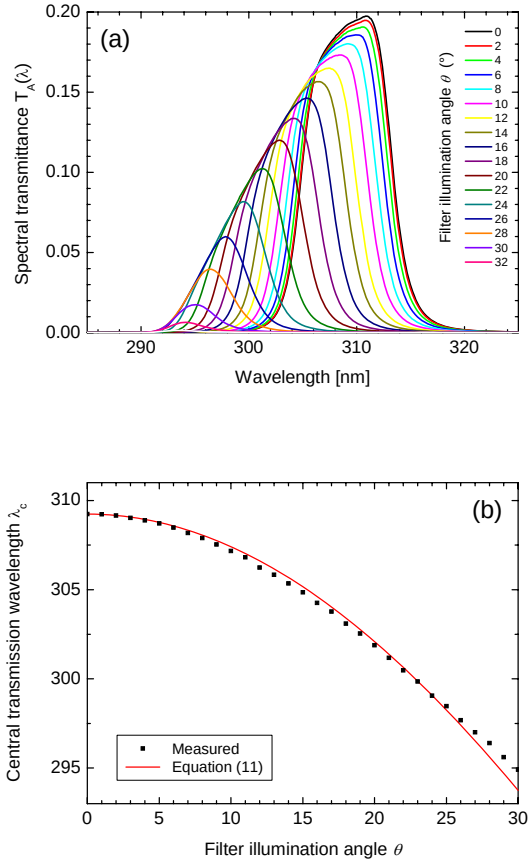

Fig. 5. **(a)** Measured relative filter transmittance $T_A(\lambda)$ as a function of the illumination angle θ. **(b)** Dots: measured central transmittance wavelength λ_c of the interference filter as a function of filter illumination angle θ. Line: central transmittance wavelength according to Eq. (11) assuming a refractive index n of 1.6 (typical value for quartz optics). The filter transmittance window shifts towards lower wavelengths if the filter is illuminated in a non-perpendicular direction (filter illumination angle $\theta \neq 0$).

2.3.2 The filter illumination angle

The central wavelength λ_c of the transmittance window of a band-pass interference filter decreases if the filter is not illuminated perpendicularly (see e.g. Lissberger and Wilcock, 1959). For incidence angles θ below ~20°, the central wavelength λ_c of the transmittance window can be approximated by the expression

$$\lambda_c(\theta) \approx \lambda_c(0°)\sqrt{1-\frac{\sin^2(\theta)}{n^2}} \approx \lambda_c(0°)\left(1-\frac{\theta^2}{2n^2}\right) \quad (11)$$

where n is the refractive index of the filter material. This relation was confirmed for the band-pass interference filters obtained for construction of the SO_2 camera prototype. Figure 5 shows the measured relative transmittance $T(\lambda)$ of the filter as a function of the illumination angle θ. The transmittance window shifts towards lower wavelengths as the illumination angle θ increases. Also, the maximum transmittance decreases and the transmission bandwidth of the filter increases slightly.

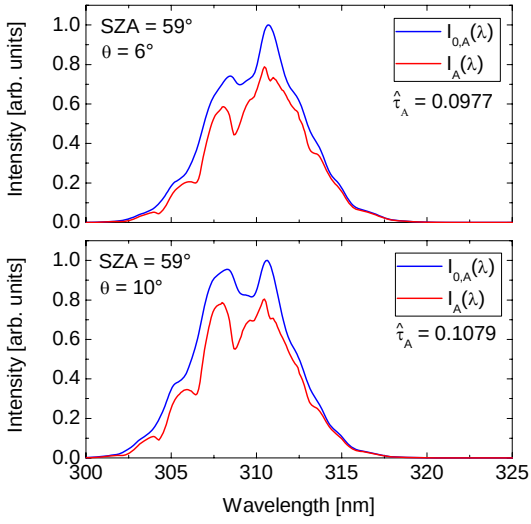

Fig. 6. Modeled light intensity I_A passing filter A of the SO_2 camera as a function of wavelength λ for two different illumination angles (θ=6° and θ=10°). The blue curve ($I_{0,A}$) assumes no SO_2 in the optical path (background spectrum), while the red curve (I_A) represents an SO_2 column density S of 400 ppmm. In both cases, the solar zenith angle (SZA) was kept at 59°. The ratio of integrated intensity under the background spectrum and under the measurement spectrum yields the indicated integrated optical density $\hat{\tau}_A$ according to Eq. 7. The two integrated optical densities $\hat{\tau}_A$ are 9% and 20% higher than for perpendicular illumination (compare to Fig. 4, top).

The dependence of the filter transmittance $T(\lambda)$ on the illumination angle can therefore change the sensitivity of the SO_2 camera to a certain SO_2 column density if the filter is not illuminated perpendicularly (θ = 0). This effect was studied using the model described in the previous section. Figure 6 depicts the modeled spectral light intensity passing filter A of the SO_2 camera under the incidence angles θ of 6° (top) and 10° (bottom). These angles correspond to a shift in the filter transmittance window of approximately 0.75 and 2 nm, respectively, towards shorter wavelengths (see Fig. 5), thus leading to a correspondingly larger influence of strong SO_2 absorption bands (located around 300 nm, see Fig. 1) on the measured weighted average optical density $\hat{\tau}_A$. This leads (in our example) to an increase in the sensitivity of the SO_2 camera (again, a constant column density of 400 ppmm was assumed). Compared to the weighted average optical density $\hat{\tau}_A$ modeled for perpendicular illumination (Fig. 4, top), an increase of 9% in $\hat{\tau}_A$ was obtained for an angle of incidence θ=6° and an increase of 20% in $\hat{\tau}_A$ was found for θ=10°. Note that while the sensitivity will generally increase towards higher incidence angles, the gradient will vary according to the position of the oscillating SO_2 absorption cross-section in relation to the transmission window (compare Fig. 1).

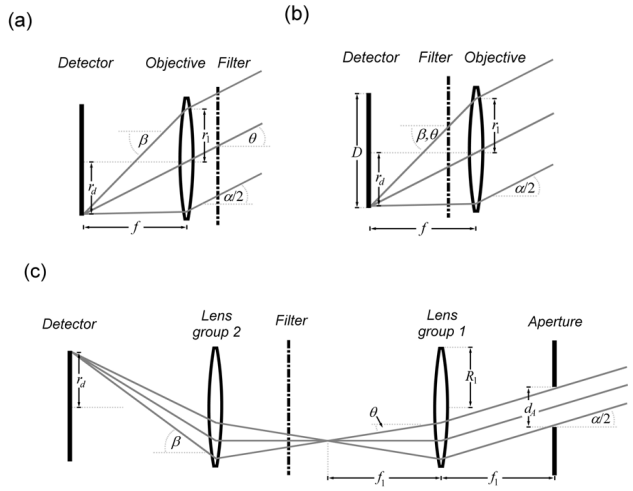

Fig. 7. Schematic of three different optical setups for SO_2 cameras. In **(a)**, the interference filter is placed in front of the object lens. In this case, the filter illumination angle θ is a function of the viewing direction and is largest close to the edge of the image. In **(b)**, the filter is positioned behind the objective. Here, a range of different angles θ are obtained for each detector pixel. Inset **(c)** shows a setup designed to minimize θ. In linear approximation, the maximum illumination angle is proportional to the ratio of the aperture size d_A to the focal length f_1 of lens group 1 in this setup.

This significant change in sensitivity for non-perpendicular illumination can make a spatially inhomogeneous calibration necessary if the angle of incidence on the filter is not equal for all measured radiation. In a simple setup of the SO_2 camera, for example, the band-pass filter may be placed in front of the camera lens (e.g. .Mori and Burton, 2006). In this configuration (shown in Fig. 7a), light originating from different areas in the field of view will pass the filter under different angles. Therefore, the sensitivity (and the proper calibration) of the SO_2 camera will depend directly on the distance r_d from the center of the image on the detector. The angle of incidence θ on the filter is fixed for each pixel on the detector in this setup. This property can be used to make a first order correction for the incidence-angle effect. However, as discussed above, the correction not only depends on θ but also on other parameters, thus rendering an exact correction difficult. The maximum filter incidence angle $\theta_{\max}$ is equal to half of the camera's total angle of view α (see Fig. 7a).

A second design approach to the optics of an SO_2 camera is to mount the interference filters between the object lens and the detector. This setup is depicted in Fig. 7b. In this configuration, the filter incidence angle θ is no longer constant for each pixel on the detector. Instead, a range of different angles are realized, thus again leading to a pixel dependent effective transmission curve. On average, the incidence angle θ is larger in this setup than if the filter is positioned in front of the lens, therefore causing a lower total transmission. However, as each pixel receives light from a range of angles, and transmission is suppressed for large angles, the wavelength shift of the effective transmission curve is also less dependent on pixel position than in the initial setup (shown in Fig. 7a). Therefore, the sensitivity of the camera is less dependent on pixel position, although the total transmission is somewhat reduced towards the edge of the detector (for large r_d) thus causing vignetting.

Aside from the two simple setups which each use only a single camera lens, a number of other designs are possible. By using multiple lenses or lens groups, an optical system can be developed that minimizes the filter illumination angle. While it is impossible to discuss here all feasible alternatives, a few general remarks can be made. An ideal optical system will conserve radiance. The radiance B entering the system is a function of the total angle of view α (B is proportional to α^2) and the first aperture in the system d_A (B is proportional to d_A^2). Once inside the system, the divergence of the light path can be decreased, but only by at the same time increasing the diameter of the apertures/optics (otherwise light is lost). Perfectly parallel propagation of light could only be achieved for optics infinitely large in diameter, or for an infinitely small aperture at the front of the system. Therefore, designing an optical system with a perpendicular filter illumination angle θ for all incident light beams is impossible. A tradeoff between perpendicular filter illumination and optical throughput (defined by the aperture and lens size) will always need to be made. Keeping in mind that the shift of λ_c is approximately proportional to θ^2 for small θ (see Eq. 11), very small angles of incidence are not required (wavelength shifts of less than 0.5 nm are obtained for $\theta < 5°$, see Fig. 5b).

One example of an optical system designed to minimize the filter illumination angle θ was developed for the SO_2 camera prototype described in Sect. 3. It is shown in Fig. 7c. While a completely parallel filter illumination is not achieved, the optical design ensures that the range of realized illumination angles is constant for all viewing directions, therefore yielding an identical effective filter transmission curve for all pixels.

It is worth mentioning another potential advantage of a nearly parallel optical path: A parallel beam allows the application of an optical filter with periodic transmittance (Fabry-Pérot etalon). Instead of using the above mentioned band-pass filters, the transmittance of a conveniently dimensioned Fabry-Perot interferometer could be tuned such that each transmittance peak lies on an absorption band of SO_2 in the wavelength range of approximately 300–315 nm (possibly pre-selected by using an additional UV transmitting, visible absorbing filter), thus greatly improving the signal to noise ratio of the measurement and making it considerably more selective to SO_2, even in the presence of other absorbers. By then slightly tilting the etalon, the transmission peaks can be shifted from the peaks to the adjacent troughs in the SO_2 absorption spectrum, thus allowing a normalization of the measurement and removal of the scattering effects as described in Sect. 2.1. A second filter is therefore not required.

2.3.3 Applying calibration corrections

Equation 8 can now be rewritten to include the effects discussed above. The physical relation between the measured weighted average optical density $\hat{\tau}_A$ and the column density of SO_2 is then given by

$$\hat{\tau}_A = -\ln\left(\frac{\int_\lambda I_S(\lambda, SZA)\cdot T_A(\lambda,\theta)\cdot Q(\lambda,\beta)\cdot T_O(r_{1..n})\cdot\exp(-\sigma(\lambda)\cdot S(\lambda))\cdot d\lambda}{\int_\lambda I_S(\lambda, SZA)\cdot T_A(\lambda,\theta)\cdot Q(\lambda,\beta)\cdot T_O(r_{1..n})\cdot d\lambda}\right) \quad (12)$$

The spectrum of incident scattered radiation I_S depends on the solar zenith angle (SZA) and on the prevailing weather conditions (clouds and fog can significantly alter I_S). Therefore, the spectrum of incident solar radiation typically changes with time. In Sect. 2.3.2, it was shown that the transmission curve of the band pass filter T_A depends on the illumination angle θ. If the effective transmission angle is not constant, this term will vary from pixel to pixel. In addition, the quantum efficiency of each pixel may vary slightly depending on the angle of incidence β (see Fig. 7). Finally, the transmission of the optical system T_O will likely be a function of the respective beam distance r from the center of the individual optical elements (vignetting caused by the individual apertures and/or the filter).

As Eq. (12) is likewise valid for calculating the weighted average optical density $\hat{\tau}_B$ in the long wave region, it represents a parameterization of the relationship between the SO_2 column density S and the measured normalized optical density. It is evident that calibration of the SO_2 camera is not trivial. In fact, due to the non-analytic integrals, the equation cannot be solved for S. While, an empirical calibration can be performed by positioning calibration cells containing known amounts of SO_2 in front of the camera (see e.g. Dalton et al., 2009), it is important to keep in mind that the calibration may depend on a number of pixel dependent parameters (e.g. θ, β, $r_{1..n}$, r_d depending on the applied optical setup) and therefore must be performed individually for each pixel on the detector.

Also, Eq. (12) shows that the relation between $\hat{\tau}$ and S is non-linear. Whether or not a linear approximation is sufficient to describe the calibration of the instrument will depend on the variability and range of encountered values for each of the parameters in the equation, and especially the range of S itself (see Dalton et al., 2009). Therefore, as many data points as possible should be collected for calibration, and these should span the entire range of measurement values.

Finally, the solar zenith angle is time dependent. Therefore, an empirical calibration using a gas cell will inevitably depend on the time of day. Fortunately, this effect is comparatively small for the typical filter configuration modeled in Sect. 2.3.1, and is not likely to be a controlling error effect for solar zenith angles smaller than 80° in similar configurations. For measurements in the early morning or late evening, however, the influence of a change in the incident spectral intensity can be significant.

3 Design of an SO_2 camera prototype

Keeping the theoretical principles described above in mind, a prototype for an advanced SO_2 camera was constructed and tested in the field. Several components (optics, filters, detector) were changed as compared to previous setups (Mori and Burton, 2006; Bluth et al., 2007) to improve the performance of the novel prototype.

3.1 Advanced optical system

An advanced optical system was designed specifically for the SO_2 camera in an attempt to reduce the illumination angle dependent calibration issues described in Sect. 2.3. A schematic of this design is shown in Fig. 7c. The optical system is composed of two lens groups between which the band-pass interference filter is located. An adjustable aperture is centered in the focal point of the first lens group. The total angle of view of the camera is therefore given by the relation

$$\alpha = 2\cdot\arctan\left(\frac{R_{\text{eff}}}{f_1}\right) \approx \frac{2R_{\text{eff}}}{f_1} \quad (13)$$

where R_{eff} is the effective radius of the first lens ($R_{\text{eff}} = R_1 - d_A/2$), f_1 is its focal length, and d_A is the diameter of the frontal aperture. Assuming the object of interest (e.g. the volcanic plume) to be at a large distance from the camera (compared to the focal lengths used in the optics), a virtual image of the viewed landscape is created in the opposite focal plane of the first lens group. The band-pass interference filter is positioned behind this image so that dust or inhomogeneities on the filter are not in focus. Behind the filter, a second group of lenses is used to project the virtual image onto the detector. The position of this lens group in relation to the detector and the virtual image can be varied such that the image is exactly scaled to fit the detector. If e.g. a 1 to 1 reproduction of the virtual image is wanted, the second lens group is placed at twice its focal length f_2 from the virtual image and the detector is likewise positioned at $2 \times f_2$ from the lens group.

The great advantage of this setup over the simple setups discussed in Sect. 2.3.2 and shown in Fig. 7a and b is that the angle of incidence θ on the band pass filter no longer varies for individual pixel positions on the detector. Although a range of illumination angles is realized, this range is identical for all pixels, thus leading to an identical effective filter transmission curve. The maximum angle of incidence $\theta_{\max}$ is controlled by the entrance aperture d_A and the focal length of the first lens group f_1, and can therefore easily be modified.

$$\theta_{\max} = \arctan\left(\frac{d_A}{2f_1}\right) \approx \frac{d_A}{2f_1} \quad (14)$$

As was discussed in Sect. 2.3.2, a perfectly parallel filter transmission cannot be realized. Equation (14) explicitly demonstrates that a reduction of the maximum illumination

angle θ_{max} can only be achieved by reducing the radiance B passing through the system. Reducing the aperture size d_A directly decreases light throughput ($B \sim d_A^2$), and an increase in f_1 results in a decrease in the total angle of view α and thus also a quadratic reduction in radiance entering the system ($B \sim \alpha^2 \sim 1/f_1^2$). For the prototype, a lens group with effective focal length f_1 of 25 mm was used and the aperture d was typically set to 2.5 mm, resulting in a maximum illumination angle θ_{max} of less than 3°, while the camera's total angle of view α was approximately 20° (the effective radius R_{eff} of the first lens was 5 mm).

Due to the relatively small aperture in the front of the optical system, the accepted radiance B was considerably lower in this optical system than in prior setups (a typical entrance aperture for a simpler setup is 25 mm). However, by using a UV-sensitive back-illuminated CCD detector instead of a standard front-illuminated chip, the signal to noise ratio was sufficient to achieve a time resolution on the order of Hz. In fact, it was found that the main limitations to measurement time resolution are the camera's digitization and readout time as well as the time required to exchange the band-pass filters, and not the exposure time itself.

3.2 Selection of the optimal band-pass filter

When selecting the band-pass interference filters for use in the SO_2 camera, several aspects must be considered. Both, the spectral position of the filter transmittance window as well as its width will determine the light throughput of the optical system. On the one hand, it can be advantageous to chose a very narrow-band transmittance window positioned directly on one of the strong SO_2 absorption lines, as the SO_2 sensitivity will be high and the calibration becomes simpler (see Sect. 2, Eq. 8 and 9). On the other hand, the light throughput of such a system will be extremely low, thus resulting in an increased relative noise level. In the following, an attempt is made to determine the ideal filter transmittance width and central wavelength λ_c for filter A. Filter B is less critical, as the incident solar radiation is much more intense above 320 nm and the instrument signal-to-noise is therefore decisively limited by filter A.

The model described in Sect. 2.3 was used to calculate the relative signal-to-noise ratio for a variety of filter configurations. The spectral transmittance curve of filter A was again parameterized using a Gaussian distribution. For transmittance FWHM between 1 and 30 nm, the relative signal-to-noise ratio was calculated as a function of the central transmittance wavelength λ_c of the filter. For the sake of comparability, an identical maximum transmittance was assumed for all filters. This can only be considered an approximation, as very narrow band-pass interference filters tend to have lower maximum transmittances than wider filters, but actual transmittances vary, so this study may represent a somewhat optimistic estimate for narrow filters. Nevertheless, it gives some guidance on how to choose optimal filter parameters. When

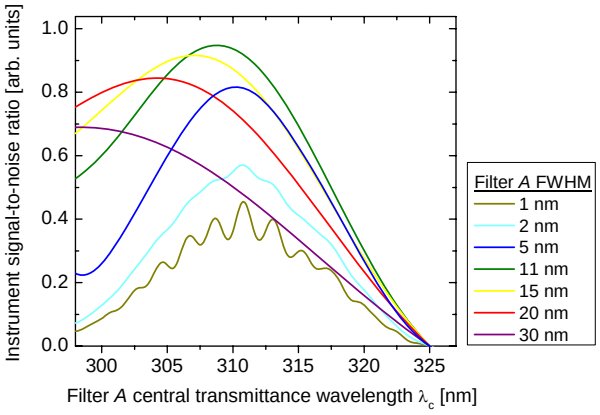

Fig. 8. Modeled instrument signal to noise ratio as a function of the central wavelength of filter A (for typical conditions, see text). Different colors represent different transmittance window FWHM. A FWHM of less than about 2 nm is needed to resolve an individual SO_2 line. However, the signal-to-noise ratio increases for larger FWHM up to a width of 11 nm due to the increased light throughput. A further increase in the FHWM of the transmittance curve degrades the signal-to-noise ratio as wavelengths are included where either no scattered radiation is available or where SO_2 exhibits only weak absorption. A broad optimum is found for a bandwidth around 11 nm and a center wavelength λ_c of about 309 nm.

comparing filters with known transmittances, further normalization of the results given in Fig. 8 by the individual maximum filter transmittances can easily be conducted. Also, a wavelength-independent detector quantum yield Q was assumed. If the quantum yield of a specific detector changes significantly over the considered wavelength interval (300 to 325 nm), the quantum efficiency curve $Q(\lambda)$ should be included in the model according to Eq. (8). Sensitivity studies showed that this can result in a slight shift in the ideal filter transmittance central wavelength λ_c (see Wöhrbach, 2008 for details).

For the calculation of instrument signal-to-noise ratio (SNR), a second filter (filter B) was simulated using a transmittance window centered at λ_c = 325 nm and an identical FWHM as filter A. The normalized weighted average SO_2 optical density $\hat{\tau}$ was then retrieved according to Quations (8) and (10), assuming an SO_2 column density of 4×10^{18} molec/cm^2, which is typical for volcanic plumes. Furthermore, as the noise of each measured integrated intensity is proportional to the square root of the intensity itself (photon statistics), the total noise of the weighted average optical density $\Delta\hat{\tau}$ could be quantified using Gaussian error propagation (see Wöhrbach, 2008 for details). Dividing $\hat{\tau}$ by $\Delta\hat{\tau}$ yields a value proportional to the SNR.

The thus obtained SNRs are shown (in arbitrary units) in Fig. 8. In general, the ideal central transmittance wavelength varies between 300 and 310 nm. Towards the shorter wavelengths, the incident scattered solar radiation $I_S(\lambda)$ decreases

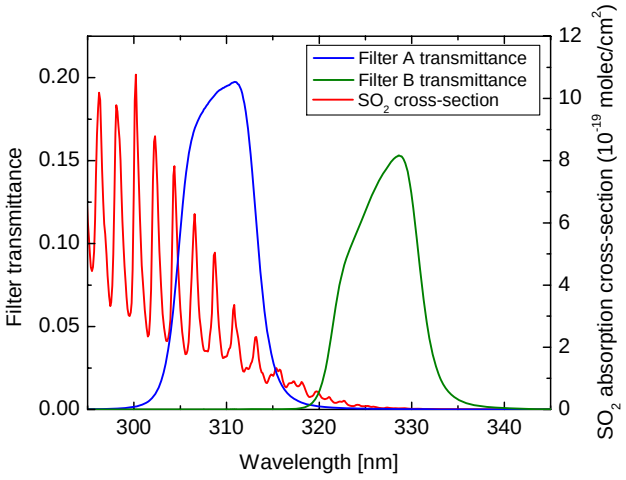

Fig. 9. Measured transmittance of the two band-pass filters used for construction of the SO_2 camera prototype. Also shown (red) is the absorption cross-section of SO_2 (Bogumil et al., 2003).

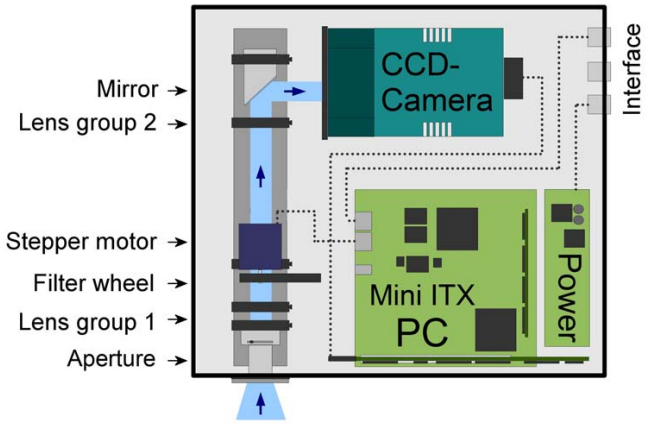

Fig. 10. Schematic setup of the SO_2 camera prototype. Light enters the instrument through an aperture, passes through the band-pass filter and is focused on the CCD detector. The measurement is controlled by an internal ITX PC, and data is saved on an internal hard drive. The interface connectors are used to configure the measurement and collect data, as well as for supply of 12 V DC power.

due to strong ozone absorption, and the relative SNR $\hat{\tau}/\Delta\hat{\tau}$ drops. Towards longer wavelengths the incident intensity $I_S(\lambda)$ increases, but the SO_2 absorption cross-section becomes smaller (see Fig. 1), therefore decreasing the measured signal and thus also lowering the SNR.

Very narrow filters (less than 2 nm) are sensitive to individual SO_2 absorption bands. For these, the calculated signal-to-noise ratio oscillates, depending on whether the transmittance window is on or between an SO_2 absorption line. If a very narrow filter were to be used, the results indicate that placing the central wavelength λ_c on the SO_2 absorption band at 311 nm would yield the highest SNR. Wider transmittance windows are no longer sensitive to individual lines, but rather to the integral over several bands. As the filter transmittance width increases, the light throughput of the system increases thereby reducing the measurement noise and increasing the signal-to-noise ratio. However, if the transmittance window becomes too wide, parts of the solar scattered radiation spectrum are included in which SO_2 absorption is less significant. Therefore, the measured signal no longer increases, and the signal-to-noise ratio decreases again.

The model indicates that the optimal filter transmittance curve $T(\lambda)$ for band-pass filters used in an SO_2 camera is centered at λ_c = 309 nm and has a FWHM of 11 nm. However, it should be noted that optical setups in which the filters are illuminated in a non-perpendicular direction will result in a shift of the effective filter transmission curve towards lower wavelengths. In such cases, the band-pass filter should be chosen such that the average effective transmission curve exhibits the optimal properties derived above. This may implicate using filters with longer maximum transmission wavelengths λ_c.

In our optical setup, the filter illumination angle θ is negligible, and the filters used for the construction of the SO_2 camera prototype were chosen according to the results described above. Figure 9 shows the transmittances of the two band-pass interference filters acquired for this purpose from BK Interferenzoptik,© Nabburg, Germany. Filter *A* was centered at 309 nm, filter *B* at 326 nm. The spectral transmittance curves $T(\lambda)$ are slightly asymmetric, with FWHM of about 10 nm.

3.3 Technical implementation

A schematic of the designed SO_2 camera prototype is shown in Fig. 10. An ANDOR© 420 BU back-thinned CCD camera was chosen as a detector. This back thinned detector features a quantum efficiency Q that is about 5 times higher at 300 nm than that of a standard front illuminated CCD ($Q \approx 0.6$). It has a wide image area of 26.6×6.7 mm (only about 11 ×6.7 mm were used) split into 1024×256 pixels, each with an area of 26 µm^2 and a well depth of 400 000 electrons. The camera is controlled by a Jetway© J7F21GE Mini-ITX PC via a PCI interface. The PC has a 1 GHz VIA© Eden processor, 1 GB RAM, and an 80 GB hard drive. It is powered off 12 V DC input voltage by an M1-ATX power supply system. The entire setup can alternatively be run off a 12 V DC power supply or a 12 V battery.

The advanced optical system depicted in Fig. 7c was constructed using 25 mm quartz lenses mounted on an adjustable OWIS© optical bench. An adjustable iris aperture was installed at the optical entrance. The entire system has an effective focal length of 24 mm and a total angle of view α of 26° (horizontal). The two filters *A* and *B* are alternatively

Fig. 11. Visible image of Mt. Etna taken on 15 October 2007 from the town of Milo, located approximately 11 km east-south-east of the volcano's summit. In this image, a dark, ash-laden plume is being emitted from the new vent on the eastern flank of the south-east crater. Plumes such as this one were intermittently emitted as a consequence of ongoing explosions at this vent.

positioned in the optical path by a Trinamic Pandrive PD1-110-42-232 stepper motor driven by a motor controller connected to the serial port of the ITX PC.

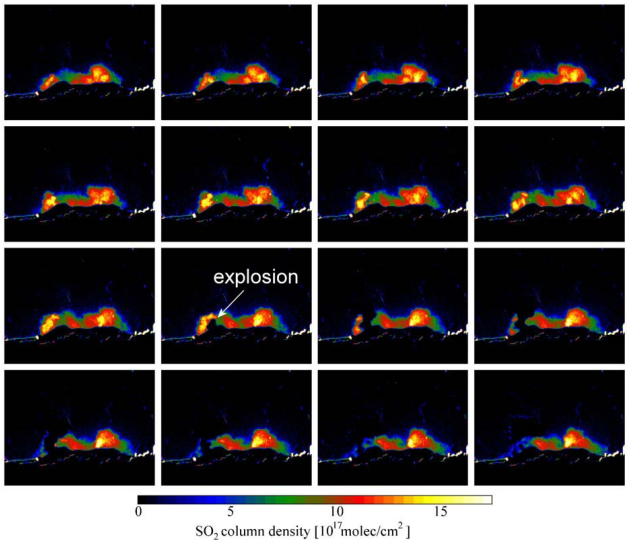

Fig. 12. Time series of SO_2 images recorded at Mt. Etna on 15 October 2007 beginning at 13:00 local time. The time gap between each of the depicted images is 21 s. In the 10th image, a dark cloud can be observed rising up from the vent on the eastern flank of the south-east crater. As UV-radiation cannot sufficiently penetrate this ash-rich plume, the signal from the volcanic plume behind the ash cloud is blocked, resulting in an area of decreased SO_2 column density.

4 Measurement examples

The designed SO_2 camera was tested in several measurement campaigns at Mt. Etna, Italy. Two interesting measurement examples will be discussed in this section. The first tests of the novel system were conducted in October of 2007. Volcanic activity at Mt. Etna was elevated during the measurement period, with a new vent opening on the eastern flank of the active south-east crater. Periodically, explosions at this vent emitted short, ash-laden gas pulses. Figure 11 shows a visible image of such an explosive event ejecting a dark ash plume.

In the first test of the instrument conducted on 15 October 2007, the SO_2 camera was used to measure the SO_2 distribution around the summit of Mt. Etna. Figure 12 shows an example time series of SO_2 images recorded from the town of Milo located about 11 km east-south-east of the volcano's summit. The field of view of the SO_2 camera coincides with that shown in Fig. 11.

The first 9 images in Fig. 12 show the slightly variable distribution of SO_2 in the summit area of Mt. Etna. On this particular day, an easterly wind was blowing the volcanic plume away from the instrument. However, it is interesting to notice the elevated SO_2 column densities around both the north-east (typically the most active) and the south-east craters. This area of elevated SO_2 is not apparent in the visible image (compare Fig. 11).

In the 10th frame shown in Fig. 12, an area of apparently reduced SO_2 can be observed on the southern side of the image. This area expands in the subsequently recorded images, and corresponds to a dark, ash-laden plume being emitted from the active vent on the eastern flank of the south-east crater (compare Fig. 11). Since UV-radiation can only partly penetrate this ash-rich plume, the enhanced signal from the volcanic plume behind the ash cloud is blocked. Therefore, the measured SO_2 column density drops to null for areas in which the ash cloud blocks the plume behind it. As the short pulse of ash-laden emissions dissipates, the original SO_2 column density can once again be measured.

This example measurement illustrates the fact that radiative transfer effects can skew or even falsify a measured SO_2 column density if they are not taken into account. The SO_2 column density along a straight line through the plume is not likely influenced by the dark ash cloud rising in front of the plume. However, the measured SO_2 value clearly decreases, as the effective light path no longer penetrates the plume. It is difficult if not impossible to correct for such effects based on the SO_2 camera data alone. However, it was recently shown that under certain conditions, the effective light path can effectively be retrieved from DOAS spectra (Kern et al., 2010). Since the errors associated with radiative transfer are among the most prominent error sources of the SO_2 camera, simultaneous measurements of the observed volcanic plume with a passive DOAS instrument are highly advantageous.

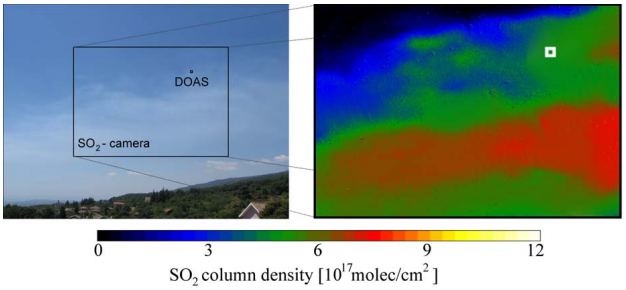

Fig. 13. Visible (left) and SO_2 camera (right) images recorded over the town of Milo at the base of Mt. Etna on 16 July 2008. The rectangle in the visible image indicates the section observed by the SO_2 camera. The images were taken in southerly direction, the plume was moving from right to left through the images. The SO_2 image was slightly smoothed to remove artifacts caused by dust in the optical system. A passive DOAS instrument was also aimed at the volcanic plume. Its approximate viewing direction is indicated by a small rectangular dot in both images.

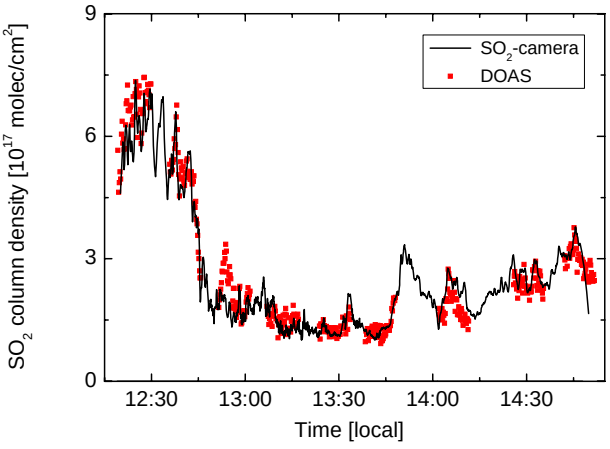

Fig. 14. SO_2 column densities measured with the passive DOAS instrument compared to those obtained in a small subsector of the SO_2 camera's field of view (after calibration with the DOAS). The time series of the subsector with the best correlation to the DOAS data is shown.

This is demonstrated in a second example. Here, a measurement conducted on 16 July 2008 at the same site in Milo is described. For this measurement, the SO_2 camera was not aimed at the volcano's summit but in a southerly direction instead. On this particular day, a westerly wind was blowing the volcanic emissions towards the east, such that they passed above and to the south of Milo. In the left side of Fig. 13, a visible image of the volcanic plume is shown. The plume can be identified by the slight white haze apparent in the center of the image. The plume was blown from right to left through the image. A large black rectangle represents the field of view of the SO_2 camera. On the right side of the image, an example SO_2 distribution measured at 12:20 local time with the SO_2 camera is shown. This image was smoothed slightly to remove artifacts caused by dust in the camera's optical system. SO_2 column densities of more than 7×10^{17} molec/cm^2 (280 ppmm) were detected in the center of the plume.

Next to the SO_2 camera, a passive DOAS instrument (NOVAC mark II, see Galle et al., 2009; Kern, 2009 for a complete description) was located on the same rooftop in Milo on 16 July 2008. For this measurement, the DOAS instrument was set to use a single, fixed viewing direction. The approximate location of this direction is given by the small rectangle in Fig. 13. However, the DOAS instrument's field of view was 0.35° which corresponds to an area of only approximately 3×3 pixels on the SO_2 camera's image.

As explained in Sect. 2, the lack of spectral resolution makes an empirical calibration of the SO_2 camera necessary. This can be achieved using calibration cells containing known SO_2 concentrations, but maintaining a constant SO_2 concentration can be difficult, as such cells tend to leak over time and, perhaps more importantly, the calibration depends on a number of time dependent parameters (see Sect. 2.3). DOAS, on the other hand, is intrinsically calibrated using literature reference spectra. However, scanning DOAS instruments are limited to a single viewing direction, so a calibration of the entire image of the SO_2 camera is not possible. Nevertheless, if a DOAS instrument is applied in parallel to measure SO_2 column densities in one point on the SO_2 camera image, this point can be used for absolute calibration and the other pixels can be calibrated relative to this point.

This technique was applied in the measurements shown in Figs. 13 and 14. As the field of view of the DOAS instrument relative to that of the SO_2 camera was not accurately known, the SO_2 camera image was divided into a large number of subsectors and an SO_2 time series spanning two hours was extracted for each subsector using a rough calibration. The subsector with the best relative correlation to the time series from the DOAS instrument was then identified, and the calibration was refined to match the intrinsic calibration of the DOAS. Finally, the calibration of the rest of the SO_2 camera's image was scaled to match the absolute calibration of the validated subsector. Calibrated in this way, the two time series showed a very good correlation, as is shown in Fig. 14. Remaining discrepancies are likely the effect of an imperfect match in field of view between the two measurements.

In this example, the advantages of calibrating the SO_2 camera with a collocated DOAS instrument become apparent. Not only is the calibration performed intrinsically with the DOAS, the calibration can also be updated constantly, and even effects caused by variable radiative transfer that are only accessible through the high resolution spectral data obtained by the DOAS can be corrected.

Perhaps the most impressive feature of the SO_2 camera is its ability to directly measure the flux of SO_2 through a certain area in the image after it is calibrated. This is made

possible by the high temporal and spatial distribution available in the SO_2 camera data which allows the tracking of inhomogeneities in the volcanic plume as they are transported downwind. Modern image processing algorithms can be set up to follow characteristic features in the volcanic plume over subsequent images, thereby giving a 2-dimensional wind field. Together with the measured SO_2 column densities, this wind field can be used to calculate the SO_2 flux through any area in the image. For calculating the volcanic emission flux, however, simpler approaches can also be applied (e.g. Mori and Burton, 2006; Bluth et al., 2007, Wöhrbach, 2008). These are analogous to the techniques used for passive DOAS measurements (e.g. described by Galle et al., 2002; Edmonds et al., 2003; Galle et al., 2009; Kern, 2009).

5 Conclusions and outlook

5.1 Features of the SO_2 camera

The introduction of the SO_2 camera concept has brought with it a new dimension to volcanic emissions monitoring. The advantages of this method over other remote sensing techniques are obvious. A 2-D image of SO_2 column densities is obtained with each measurement. While such images have been compiled in the past using the imaging DOAS method (Bobrowski et al., 2006, Louban et al., 2009), the time needed to record a 2-D image with this technique is around 15 min. In presently available SO_2 cameras, the time resolution is on the order of seconds and could be further improved by using back-illuminated detectors and a Fabry-Pérot etalon instead of band-pass interference filters (as described in Sect. 2.3.2). At the same time, the increased signal-to-noise ratio allows the technique to be readily applied to SO_2 plumes of lesser concentration, e.g. industrial or power plant stacks (see e.g. Wöhrbach, 2008; Dalton et al., 2009).

Multiple, sequentially recorded DOAS measurements need to be interpolated and integrated when calculating the amount of SO_2 in the cross-section of a volcanic plume. For emission flux calculation, this value is subsequently multiplied by the wind speed at plume height, which itself is either retrieved from other DOAS measurements (see e.g. McGonigle et al., 2005; Fickel, 2008, Galle et al., 2009; Johansson et al., 2009b) or taken from an external source. This procedure is greatly simplified for the SO_2 camera. Here, the SO_2 column density can be integrated along any line of pixels in a single image, directly yielding the SO_2 amount along this line. By choosing a line perpendicular to the plume's movement direction, the SO_2 amount in the plume cross-section can thus be calculated from a single image. The plume speed can then be determined by observing the movement of characteristic plume inhomogeneities in subsequent images. Together, the volcanic emission flux is thus directly obtained from the SO_2 camera's data without the necessity of any additional information.

5.2 Limitations of SO_2 cameras

Despite the major advantages of the technique over other remote sensing measurements (DOAS, FTIR), there are also several limitations. High resolution spectroscopic techniques are able to identify different absorbers by their characteristic absorption structures. Therefore, these instruments can measure multiple components simultaneously, even if their narrow-band absorption lines are located in the same wavelength range. For example, DOAS can distinguish between SO_2 and O_3 absorption, as well as separate BrO and NO_2 structures. The principle of the SO_2 camera, on the other hand, will only yield correct results if SO_2 is by far the strongest narrow-band absorber in the wavelength interval used for the measurement. This condition is usually fulfilled in volcanic plumes, but it disqualifies the technique for use in applications in which this is not the case. Also, while the design of similar instruments for the measurement of other species is in principle possible, this condition is not fulfilled for any other volcanic emission product in the UV wavelength range. As helpful as it would be, the construction of a BrO-camera using the same techniques is likely to fail in volcanic plume environments.

The second limitation of the SO_2 camera is its difficult calibration. The incident radiation intensity $I(\lambda)$ is not measured as a function of wavelength λ, but instead integrated over the entire transmittance window of the band-pass interference filter (I_M is obtained, see Eq. 5). Therefore, the optical density $\tau(\lambda)$, which is proportional to the SO_2 column density S (Eq. 4) can not be retrieved. Instead, a weighted average optical density $\hat{\tau}$ is obtained (Eq. 8). The relationship between $\hat{\tau}$ and S is not linear and the calculation of a calibration coefficient can be complex. As described in Sect. 2.3, the calibration depends on the solar zenith angle (SZA), the total O_3 column, the filter illumination angle θ, and the SO_2 column density S itself.

Lastly, the column densities measured with the SO_2 camera (or any other remote sensing instrument that uses scattered solar radiation as a light source) can be largely influenced by radiative transfer effects. Two competing effects are known. For one, radiation scattered into the instrument's line of sight between the volcanic plume and the instrument itself can cause a "dilution" of the measured SO_2 signal. On the other hand, multiple scattering on aerosols and water droplets in the volcanic plume can extend the average optical path in the plume, thus enhancing the measured SO_2 column density. Kern et al., (2010) have shown that these effects can greatly influence the retrieved column densities, possibly skewing them by more than a factor of 3 under certain conditions.

Table 1. Overview of the different error sources inherent in SO_2 camera measurements and the approximate magnitude of the associated errors. Also given are methods to correct for the errors if possible.

Error source	Approximate error	Correction method	Reference
Use of only 1 filter, no normalization for aerosol scattering & absorption	Small for aerosol-free plumes (very rare), otherwise up to several hundred percent	Normalize the optical density by using a second filter centered at around 325 nm	Sect. 2.1
Imperfect correction of scattering/absorption effects by use of a second wavelength channel	Typically <5% if the second channel is shifted by ∼15 nm to longer wavelengths; up to 10% for very fine aerosols	This is an intrinsic problem with the method and cannot be quantitatively corrected without additional information	Sect. 2.1
Changing background spectral intensity I_S	Below 10% for low solar zenith angles and clear background, can be much higher for large SZAs or variable clouds behind plume	Frequent recording or calculation of background image	Sect. 2.2, Sect. 2.3.1
Non-perpendicular illumination of filters	Typically about 2%/° deviation from perpendicular direction	Separate calibration for each individual pixel in the image	Sect. 2.3.2
Use of a linear calibration $\hat{\tau} \sim S$ obtained by using calibration cells	Small for column densities below 4×10^{18} molec/cm^2, otherwise easily 50% or more	Use of calibration cells with similar column densities as in the measurement	Sect. 2.3.3, Dalton et al., 2009
Uncertainty in radiative transfer	Typically ∼30% for volcanic plumes, 70% or more in extreme cases (high SO_2 and aerosol/ash loads, large distance from plume)	Retrieval of effective photon path length from moderate resolution spectra recorded by collocated DOAS instrument	Kern et al., 2010

5.3 Overcoming some of the limitations

The SO_2 camera is a novel technology that brings with it a vast variety of applications. However, both the technical implementation of the instrument as well as the data retrieval procedures are still in an early stage of development. Several advances along both lines were made in the scope of this study. The optical system described in Sect. 3.1 greatly reduces the dependence of the instrument sensitivity on the viewing direction. The use of a back-illuminated CCD detector and the associated increase in quantum efficiency (factor of 5) enhances the signal-to-noise ratio of a given incident radiation intensity by more than a factor of 2 compared to front-illuminated chips. Finally, the maximum possible sensitivity was achieved by selecting filters according to the theoretical considerations explained in Sect. 3.2.

On the data retrieval side, a model was used to describe the difficulties involved in calibrating the SO_2 camera. This or similar models can be used to simulate the exact influence of the measurement parameters (solar zenith angle, stratospheric O_3 column, illumination angle and SO_2 column density) on the measured integrated optical density $\hat{\tau}$ for a specific SO_2 camera design. Instead of using a fixed linear relationship between the integrated optical density $\hat{\tau}$ and the column density S, a lookup table could be computed from Eq. (12) giving much more accurate results.

Empirical calibration will likely continue to be of great value. However, instead of calibrating the camera with SO_2 cells, an up-to-date intrinsic calibration can be obtained by co-locating a DOAS instrument with the SO_2 camera (see Sect. 4). In this manner, the 2-D SO_2 distributions measured with the camera can be normalized using the high resolution spectroscopic measurements conducted in one subsector of the camera's field of view. Aside from giving an accurate calibration, the recent advances in retrieving the radiative transfer in and around volcanic plumes (Kern et al., 2010) can thus be applied to SO_2 camera measurements. An overview of all the examined error sources and magnitudes of the associated errors is given in Table 1, along with methods for correcting the errors in cases where this is possible.

5.4 Future work

Having implemented the solutions described above, the potential of the SO_2 camera for volcanic emissions research is enormous. The instrument gives 2-D SO_2 distributions at time resolutions on the order of 1 Hz or better. The relatively low cost of the instrument (order of 20 000 €) makes the SO_2 camera an ideal tool for the real-time monitoring of volcanic activity. Most volcano observatories already have visible and IR cameras permanently observing potentially active volcanoes. Adding an SO_2 camera instantly gives an overview of gas emissions, even to the untrained observer. Also, the obtained images allow a detailed analysis of the dynamic interaction of volcanic gas with the atmosphere in the wake of the emission crater.

However, the possibilities go far beyond simple visible observation. Fundamental digital image processing algorithms can be applied to retrieve the SO_2 flux through any line in the image (see e.g. Mori and Burton, 2006; Bluth et al., 2007; Wöhrbach, 2008). But the information content of the measured series of images is much greater than is often realized. Modern motion correspondence algorithms (see e.g. Cox, 1993; Jähne, 2002) should even allow the calculation of a 2-D projection of the 3-D wind field in the wake of the volcano (multiple cameras could even give 3-D wind fields, see below). Such data is interesting from a meteorological standpoint, as volcanoes often represent significant topographical perturbations in regional wind fields. Also, spatial variations in the wind speed and direction can influence the accuracy of volcanic emission fluxes measured downwind of the volcano by scanning or traverse remote sensing techniques. Therefore, integrating SO_2 camera results in other gas emission flux retrievals could help constrain wind speed and direction and thus yield more accurate determinations of gas emission fluxes.

Finally, the relatively low cost of the instrument makes the deployment of multiple instruments possible. If several SO_2 cameras are used to view a volcanic plume from different locations simultaneously (or sequentially from a mobile platform), a tomographic reconstruction could help gain insights into the 3-dimensional plume distribution and its temporal evolution. Such inversions have already been performed for volcanic plumes in the past using passive DOAS instruments (Kazahaya et al., 2008; Wright et al., 2008; Johansson et al., 2009a), but they are inherently ill-constrained due to the very limited amount of measurement geometries available. As a single SO_2 camera image contains as many viewing directions as the sensor has pixels, the problem quickly becomes better constrained, and the influence of a-priori assumptions is reduced. For all of the above reasons, the SO_2 camera may well become the standard instrument most frequently applied worldwide for volcanic emissions measurements in the foreseeable future.

Acknowledgements. We would like to thank Fred Prata and an anonymous reviewer for their detailed reviewing and help in improving the manuscript. We also thank Nicole Bobrowski, Fabio Vita, Salvatore Inguaggiato and Tommaso Caltabiano for their logistical support during the measurements.

Edited by: S. Slijkhuis

References

Bluth, G. J. S., Shannon, J. M., Watson, I. M., Prata, A. J., and Realmuto, V. J.: Development of an ultra-violet digital camera for volcanic SO_2 imaging, J. Volcanol. Geotherm. Res., 161, 47–56, 2007.

Bobrowski, N., Hönninger, G., Galle, B., and Platt, U.: Detection of bromine monoxide in a volcanic plume, Nature 423, 273–276, 2003.

Bobrowski, N., Hönninger, G., Lohberger, F., and Platt, U.: IDOAS: A new monitoring technique to study the 2D distribution of volcanic gas emissions, J. Volcanol. Geotherm. Res., 150, 329–338, 2006.

Bogumil, K., Orphal, J., Homan, T., Voigt, S., Spietz, P., Fleischmann, O., Vogel, A., Hartmann, M., Bovensmann, H., Frerick, J., and Burrows, J.: Measurements of molecular absorption spectra with the SCIAMACHY pre-flight model: instrument characterization and reference data for atmospheric remote-sensing in the 230–2380 nm region, J. Photochem. Photobiol. A., 157, 167–184, 2003.

Burton, M. R., Allard, P., Murè, F., and La Spina, A.: Magmatic gas composition reveals the source depth of slug-driven Strombolian explosive activity, Science, 317, 227–230, 2007.

Cox, I. J.: A Review of Statistical Data Association Techniques for Motion Correspondence, Int. J. Comput. Vision., 10, 53–66, 1993.

Dalton, M. P., Watson, I. M., Nadeau, P. A., Werner, C., Morrow, W., and Shannon, J. M.: Assessment of the UV camera sulfur dioxide retrieval for point source plumes, J. Volcanol. Geoth. Res., 188, 358–366, 2009.

Edmonds, M., Herd, R. A., Galle, B., and Oppenheimer, C.: Automated, high time-resolution measurements of SO_2 flux at Soufrière Hills Volcano, Montserrat. Bull. Volcanol., 65, 578–586, 2003.

Fickel, M.: Measurement of trace gas fluxes from point sources with Multi-Axis Differential Optical Absorption Spectroscopy, Diploma thesis, University of Heidelberg, 105 pages, Heidelberg, 2008.

Galle, B., Johansson, M., Rivera, C., Zhang, Y., Kihlman, M., Kern, C., Lehmann, T., Platt, U., Arellano, S., Hidalgo, S., Network for Observation of Volcanic and Atmospheric Change (NOVAC) – A global network for volcanic gas monitoring: Network layout and instrument description, J. Geophys. Res., 115, D05304, doi:10.1029/2009JD011823, 2010.

Galle, B., Oppenheimer, C., Geyer, A., McGonigle, A. J. S., Edmonds, M., and Horrocks, L.: A miniaturized ultraviolet spectrometer for remote sensing of SO_2 fluxes: A new tool for volcano surveillance, J. Volcanol. Geotherm. Res., 119, 241–254, 2002.

Götz, F. W. P.: Zum Strahlungsklima des Spitzbergensommers. Strahlungs- und Ozonmessungen in der Königsbucht 1929, Gerl Beitr Geophys 31, 119–154, 1931.

Götz, F. W. P.: Meetham AR, Dobson GMB, The vertical distribution of ozone in the atmosphere, Proc. Roy. Soc. A., 145, 416–446, 1934.

Jähne, B.: Digitale Bildverarbeitung (Digital Image Processing), Springer Verlag, Heidelberg, 2002.

Johansson, M., Galle, B., Rivera, C., and Zhang, Y.: Tomographic Reconstruction of Gas Plumes Using Scanning DOAS, Bull. Volcanol., 71, 1169–1178, doi:10.1007/s00445-009-0292-8, 2009a.

Johansson, M., Galle, B., Zhang, Y., Rivera, C., Chen, D., and Wyser, K.: The Dual-Beam mini-DOAS technique - measurements of volcanic gas emission, plume height and plume speed with a single instrument, Bull. Volcanol., 71, 747–751, doi:10.1007/s00445-008-0260-8, 2009b.

Kazahaya, R., Mori, T., Kazahaya, K., and Hirabayashi, J.: Computed tomography of SO_2 concentration distribution in the volcanic plume of Miyakejima, Japan, by airborne traverse technique using three UV spectrometers, Geophys. Res. Lett., 35, L13816, doi:10.1029/2008GL034177, 2008.

Kern, C.: Spectroscopic measurements of volcanic gas emissions in the ultra-violet wavelength region. Ph.D. thesis, University of Heidelberg, pages, Heidelberg, http://www.ub.uni-heidelberg.de/archiv/9574, 2009.

Kern, C., Sihler, H., Vogel, L., Rivera, C., Herrera, M., and Platt, U.: Halogen oxide measurements at Masaya volcano, Nicaragua using active long path differential optical absorption spectroscopy, Bull. Volcanol., 71, 659–670, doi:10.1007/s00445-008-0252-8, 2009.

Kern, C., Deutschmann, T., Vogel, L., Wöhrbach, M., Wagner, T., and Platt, U.: Radiative transfer corrections for accurate spectroscopic measurements of volcanic gas emissions, Bull. Volcanol., 72, 233–247, doi:10.1007/s00445-009-0313-7, 2010.

Kick, F.: A UV camera for the measurement of atmospheric trace gas distributions (translated from German), Undergraduate thesis, University of Heidelberg, 101 pp., Heidelberg, 2008.

Lissberger, P. H. and Wilcock, W. L.: Properties of All-Dielectric Interference Filters. II. Filters in Parallel Beams of Light Incident Obliquely and in Convergent Beams, J. Opt. Soc. Am., 49, 126–128, 1959.

Lohberger, F., Hönninger, G., and Platt, U.: Ground-based imaging differential optical absorption spectroscopy of atmospheric gases, Appl. Opt., 43, 4711–4717, 2004.

Louban, I., Bobrowski, N., Rouwet, D., Inguaggiato, S., and Platt, U.: Imaging DOAS for volcanological applications, Bull. Volcanol., 71, 753–765, doi:10.1007/s00445-008-0262-6, 2009.

McGonigle, A. J. S., Delmelle, P., Oppenheimer, C., Tsanev, V. I., Delfosse, T., Horton, H., Williams-Jones, G., and Mather, T. A.: SO_2 depletion in tropospheric volcanic plumes, Geophys. Res. Lett., 31, L13201, doi:10.1029/2004GL019990, 2004.

McGonigle, A. J. S., Inguaggiato, S., Aiuppa, A., Hayes, A. R., and Oppenheimer, C.: Accurate measurement of volcanic SO_2 flux: Determination of plume transport speed and integrated SO_2 concentration with a single device, Geochem. Geophys. Geosyst., 6, Q02003, doi:10.1029/2004GC000845, 2005.

Moffat, A. J. and Millán, M. M.: The applications of optical correlation techniques to the remote sensing of SO_2 plumes using sky light, Atmos. Environ., 5, 77–690, 1971.

Mori, T. and Burton, M. R.: The SO_2 camera: a simple, fast and cheap method for ground-based imaging of SO_2 in volcanic plumes, Geophys. Res. Lett., 33, L24804, doi:10.1029/2006GL027916, 2006.

Mori, T. and Burton, M. R.: Quantification of the gas mass emitted during single explosions on Stromboli with the SO_2 imaging camera, J. Volcanol. Geoth. Res., 188, 395–400, 2009.

Oppenheimer, C., Francis, P., Burton, M. R., Maciejewski, A. J. H., and Boardman, L.: Remote measurement of volcanic gases by Fourier transform infrared spectroscopy, Appl. Phys. B, 67, 505–515, 1998a.

Oppenheimer, C., Francis, P., and Stix, J.: Depletion rates of sulfur dioxide in tropospheric volcanic plumes, Geophys. Res. Lett., 25, 2671–2674, 1998b.

Oppenheimer, C., Kyle, P. R., Tsanev, V. I., McGonigle, A. J. S., Mather, T. A., and Sweeney, D.: Mt. Erebus, the largest point source of NO_2 in Antarctica, Atmos. Environ., 39, 6000–6006, 2005.

Platt, U. and Stutz, J.: Differential Optical Absorption Spectroscopy – Principles and Applications, Springer, Berlin, Heidelberg, New York, 2008.

Rodríguez, L. A., Watson, I. M., Edmonds, M., Ryan, G., Hards, V., Oppenheimer, C., and Bluth, G. J. S.: SO_2 loss rates in the plume emitted by Soufrière Hills volcano, Montserrat, J. Volcanol. Geotherm. Res., 173, 135–147, 2008.

Spinetti, C. and Buongiornio, M. F.: Volcanic aerosol optical characteristics of Mt. Etna tropospheric plume retrieved by means of airborne multispectral images, J. Atmos. Sol. Terr. Phys., 69, 981–994, 2007.

Stoiber, R. E., Malinconico, L. L., and Williams, S. N.: Use of the correlation spectrometer at volcanoes, edited by: Tazieff, H. and Sabroux, J. C., Forecasting volcanic events, Elsevier, Amsterdam, 424–444, 1983.

Voigt, S., Orphal, J., Bogumil, K., and Burrows, J. P.: The temperature dependence (203-293K) of the absorption cross sections of O_3 in the 230–850 nm region measured by Fourier-transform spectroscopy, J. Photochem. Photobiol. A., 143, 1–9, 2001.

Wöhrbach, M.: Further development and testing of a UV-camera for the determination of trace gas distributions (translated from German), Diploma thesis, University of Heidelberg, 151 pages, Heidelberg, Germany, 2008.

Wright, T. E., Burton, M. R., Pyle, D. M., and Caltabiano, T.: Scanning tomography of SO_2 distribution in a volcanic gas plume, Geophys. Res. Lett., 35, L17811, doi:10.1029/2008GL034640, 2008.